Original Paper

Numerical analysis of matrix swelling and its effect on microstructure of digital coal and its associated permeability during CO$_2$-ECBM process based on X-ray CT data

Hui-Huang Fang [a, b, *], Zhang-Fei Wang [a, b, *], Shu-Xun Sang [c, d, e], Yan-Hui Huang [a, f]

[a] School of Earth and Environment, Anhui University of Science and Technology, Huainan, Anhui, 232001, China
[b] Institute of Energy, Hefei Comprehensive National Science Center, Hefei, Anhui, 230000, China
[c] Low Carbon Energy Institute, China University of Mining and Technology, Xuzhou, Jiangsu, 221008, China
[d] School of Resources and Geosciences, China University of Mining and Technology, Xuzhou, Jiangsu, 221116, China
[e] Jiangsu Key Laboratory of Coal-based Greenhouse Gas Control and Utilization, China University of Mining and Technology, Xuzhou, Jiangsu, 221008, China
[f] State Key Laboratory of Petroleum Resources and Prospecting, China University of Petroleum, Beijing, 102249, China

ARTICLE INFO

ABSTRACT

Matrix swelling effect will cause the change of microstructure of coal reservoir and its permeability, which is the key factor affecting the engineering effect of CO$_2$-ECBM technology. The Sihe and Yuwu collieries are taken as research objects. Firstly, visualization reconstruction of coal reservoir is realized. Secondly, the evolution of the pore/fracture structures under different swelling contents is discussed. Then, the influence of matrix phase with different swelling contents on permeability is discussed. Finally, the mechanism of swelling effect during the CO$_2$-ECBM process is further discussed. The results show that the intra-matrix pores and matrix-edge fractures are the focus of this study, and the contacting area between matrix and pore/fracture is the core area of matrix swelling. The number of matrix particles decreases with the increase of size, and the distribution of which is isolated with small size and inter-connected with large size. The swelling effect of matrix particles with larger size has a great influence on the pore/fracture structures. The number of connected pores/fractures is limited and only interconnected in a certain direction. With the increase of matrix swelling content, the number, porosity, width, fractal dimension, surface area and volume of pores/fractures decrease, and their negative contribution to absolute permeability increases from 0.368% to 0.633% and 0.868%-1.404%, respectively. With the increase of swelling content, the number of intra-matrix pores gradually decreases and the pore radius becomes shorter during the CO$_2$-ECBM process. The matrix continuously expands to the connected fractures, and the width of connected fractures gradually shorten. Under the influence of matrix swelling, the bending degree of fluid flow increases gradually, so the resistance of fluid migration increases and the permeability gradually decreases. This study shows that the matrix swelling effect is the key factor affecting CBM recovery, and the application of this effect in CO$_2$-ECBM process can be discussed.
© 2023 The Authors. Publishing services by Elsevier B.V. on behalf of KeAi Communications Co. Ltd. This is an open access article under the CC BY-NC-ND license (http://creativecommons.org/licenses/by-nc-nd/4.0/).

1. Introduction

The CO$_2$ geological storage and enhanced coal bed methane recovery (CO$_2$-ECBM) technology has dual advantages of energy and environment (Fang et al., 2021; Yang et al., 2021). While enhancing CH$_4$ recovery to increase CBM production, this technology can also sequester CO$_2$ to reduce greenhouse gas emissions in the atmosphere (Fang et al., 2019a; Zhang et al., 2021a). A series of CO$_2$-ECBM demonstration projects successively carried out by various countries have made important progress in the effectiveness study of the CO$_2$-ECBM (Fujioka et al., 2010; Bustin et al., 2016), which focuses on CO$_2$ injection, storage mechanism and capacity, and CH$_4$ stimulation effect (Li et al., 2020a; Zheng et al., 2020). The changes of permeability caused by competitive adsorption of CO$_2$ and CH$_4$ after CO$_2$ injected are key to the commercialization of CO$_2$-ECBM engineering.

---

* Corresponding authors. Anhui University of Science and Technology, China.
E-mail addresses: huihuangfang@aust.edu.cn (H.-H. Fang), wzf612429@163.com (Z.-F. Wang).

The CO_2-ECBM process is accompanied not only by mass transfer between substances of different phases (Yang et al., 2021), but also by competitive adsorption between CH_4 and CO_2 (Sun et al., 2018; Yang et al., 2021). Compared with CH_4, coal matrix has higher physical adsorption affinity for CO_2 (Guo et al., 2018; Hu et al., 2019). The molar adsorption capacity of the matrix for CO_2 is twice that of CH_4, and the volumetric adsorption capacity ratio for CO_2 is about 5 times that of CH_4 (Luo et al., 2019; Long et al., 2021), and this ratio will be further improved under supercritical conditions (i.e., Pressure is greater than 7.3 MPa and temperature is higher than 31.5 °C), which will result in the matrix swelling and further lead to the permeability change (Li et al., 2021; Wei et al., 2021). Therefore, it is very important to accurately quantify the matrix swelling effect on permeability after CO_2 injection.

The influence of matrix swelling on porosity and permeability can be indirectly reflected in the alteration of pore/fracture structures. Compared with the fluid as medium to explore matrix swelling effect (Zhang et al., 2021b; Zeng et al., 2021), the X-ray computer tomography (CT) technology has significant advantages (Hao et al., 2020; Wang et al., 2021a). Based on X-ray CT technology, the 3D visualization reconstruction and quantitative analysis of matrix swelling effect can be achieved (Fang et al., 2020; Li et al., 2020b), and the geometric (i.e., Radius, area, volume et al.) and topological (i.e., Coordination number, Connectivity function et al.) changes of pore/fracture network under different matrix swelling contents can be further visualized (Fang et al., 2020; Zhu et al., 2020). After CO_2 is injected into reservoir, the influence of matrix with different scales, shapes, scales and spatial distribution on pore/fracture structures under different swelling contents can be clarified, which is the latest research idea in digital core for digital reconstruction and characterization of matrix swelling effect in CO_2-ECBM process.

In order to quantitatively and intuitively analyze the pore/fracture structure characteristics caused by matrix swelling, and then the changes of permeability, the Sihe (SH) and Yuwu (YW) mining area in Qinshui basin were taken as research objects in this study. Firstly, the quantitative analysis of coal reservoir was realized. Secondly, the visualization reconstruction of matrix swelling effect based on image processing technology was realized, and the evolution of pore/fracture structures under different swelling contents was discussed. Then, the analysis of geological and mathematical model for permeability calculation with pore/fracture structure network as geological carrier was realized, and the influence of matrix on permeability under different matrix swelling contents was discussed. Finally, the application and mechanism of matrix swelling effect during the CO_2-ECBM process were further discussed.

The innovations of this study are mainly reflected in the following aspects: (1) The visualization reconstruction of matrix swelling effect based on image processing technology is realized; (2) The evolution of pore/fracture structure under different swelling contents is discussed; (3) The influence of matrix on porosity and permeability under different matrix swelling contents is discussed; (4) The application and mechanism of matrix swelling effect in CO_2-ECBM process are discussed. This study shows that matrix swelling effect is the key factor affecting the engineering realization of CO_2-ECBM technology.

2. Samples and methods

2.1. Sample collection and basic testing

The No. 15 coal seam of Taiyuan Formation and No. 3 coal seam of Shanxi Formation in Qinshui Basin are the main gas-bearing reservoirs (Zhang et al., 2019a; Hou et al., 2020; Fang et al., 2021),

and the experimental samples were taken from the fresh working face of SH and YW mining areas in this area with the sampling depth of 200—800 m (Fig. 1). The fresh coal samples collected require specific anti-oxidation treatment (Fig. 1c), and the sample preparation should be carried out in accordance with the corresponding national standard (i.e. GB/T 6948—2008 and GB/T 8899-2013; Liu et al., 2017; Fang et al., 2019b; Fang et al., 2021).

The maximum vitrinite reflectance was determined according to the national standard with GB/T 6948-2008 (Fang et al., 2021; Feng et al., 2021), the proximate analysis follows the national standard of GB/T 30732-2014 (Liang et al., 2021), and the maceral analysis was carried out according to the national standard with GB/T 8899-2013 (Wu et al., 2021). Table 1 shows the key properties of coal samples used in this study. The maximum vitrinite reflectance of two samples ranges from 2.19% to 3.33%, which are anthracite. The coal samples are mainly bright coal, followed by dark coal, which belongs to semi-bright coal, and the vitrinite is the main organic component (Table 1).

2.2. Sample scanning and visualization analysis

2.2.1. Sample scanning

The two samples scanned by X-ray CT technology are small coal pillars with a diameter of 2 mm and a height of about 6 mm drilled in a coal pillar with a diameter of 2 cm and a height of 5 cm (Fig. 2a). The X-ray source, precision sample table, high resolution detector, data processing system and controller system are the main controls of this scanning and imaging system used in this study (Fig. 2b; Fang et al., 2020, 2021) The gray, black and white areas respectively represent the distribution of organic matter, pores/fractures and minerals (Fig. 2c).

In this study, the scanning resolution is 1.00 μm, the 990 non-destructive 2D CT slices with each layer of 988 × 1013 voxels were obtained from SH sample, and the 990 non-destructive 2D CT slices with each layer of 988 × 1014 voxels were also obtained from YW sample (Table 2).

2.2.2. Visualization analysis

On the basis of considering the computer memory and running speed, in order to eliminate the influence of background edges, CT slices were cut into cubes with sides of 600 voxels according to their respective effective regions (Fig. 3a), which were the regions of interest for this image analysis. In order to obtain reliable information on the image, the median filtering algorithm can be used to filter the original CT slices (Fig. 3b; Li and Zhang, 2019; Jing et al., 2021). The watershed algorithm is adopted to determine the segmentation threshold with good recognition ability for weak edges (Fang et al., 2021; Wang et al., 2021b), and the pore/fracture, matrix and mineral components can be respectively extracted in digital coal (Fig. 3c). The representative elementary volume (REV) can effectively reduce the amount of computer memory and speed up the calculation (Ni et al., 2017; Wang et al., 2019). The RVE size can be determined by analyzing the change law of porosity and RVE size, that is, when porosity does not change any more, the corresponding RVE is used as the RVE of the whole digital coal (Fig. 3d).

2.3. Numerical analysis of matrix swelling process

During the matrix swelling process, the pixel value in matrix is set to the maximum pixel value in the neighborhood. The matrix swelling process will firstly fill small pores in matrix (i.e. the B_2 region in Fig. 4a and 4b), and the indentation at the boundary in binary image will continue to amplify particle size and may connect adjacent particles to the matrix (i.e. the B_1 and B_3 region in Fig. 4a and 4b). Specifically, in the original input image, the swelling of
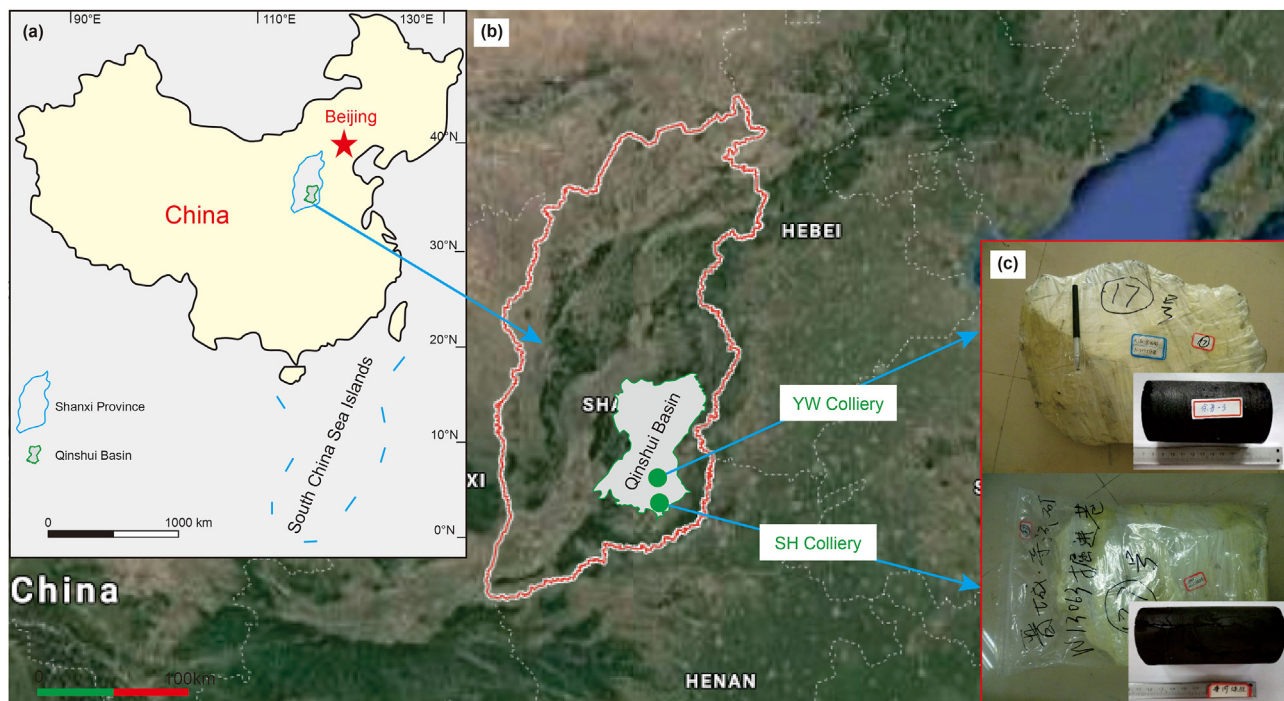
Fig. 1. Sampling point distribution of experimental samples. (a) Location of the Shanxi province in China; (b) Location of the Qinshui Basin in China and the distribution of sampling point, and (c) Anti-oxidation treatment of coal sample.

Table 1
Key properties of two coal samples used in this study.

Sampling location	$R_{o,max}$, %	Proximate analysis, wt. %				Macerals analysis, vol. %		
		M_{ad}	A_{ad}	V_{daf}	FC_{ad}	Vit	Ine	Min
SH	3.33	1.48	13.12	6.32	81.39	79.84	18.36	1.80
YW	2.19	1.10	11.98	13.44	76.19	73.16	23.66	3.18

Notes: wt. %, weight percent; vol. %, volume percentage; $R_{o,max}$, maximum vitrinite reflectance; M_{ad}, moisture; A_{ad}, ash yield; V_{daf}, volatile matter; FC_{ad}, fixed carbon content; "ad", air-drying base; "daf", dry ash-free basis; Vit, vitrinite content; Ine, inertinite content; Min, mineral content.

matrix element A first fills its internal pore B_2 and then its marginal portion B_3. When the matrix expands to a certain extent, the pores and fractures between matrix element A and matrix elements B_1 and B_3 will be filled (Fig. 4).

Previous studies show that the volumetric swelling rate of CH_4 and CO_2 adsorbed by reservoir is between 0.2% and 1.6% under conventional temperature and pressure conditions (George and Barakat, 2001; Majewska and Zietek, 2007; Zhu et al., 2020). Therefore, in this numerical simulation, the matrix swelling content can be set as 0.3%, 0.6%, 0.9%, 1.2% and 1.5% respectively, and the matrix swelling process can be controlled by combining porosity. The segmentation threshold of pores/fractures under different swelling contents of SH and YW samples are shown in Table 3.

In this study, firstly, the pores/fractures can be extracted from the selected REV and the initial porosity can be calculated. Secondly, the corresponding porosity under different matrix swelling contents can be calculated, and the segmentation threshold of pore/fracture can be pushed back according to the porosity under different swelling contents. Then, pores/fractures can be extracted and their connectivity can be analyzed based on the newly determined threshold value. Finally, the controlling effect of pore/fracture structure evolution on permeability can be quantitatively analyzed (Fig. 5).

2.4. Connectivity analysis of microstructures of digital coal

The connectivity of pore/fracture space is an important topological information of porous media, which will affect the physical properties of porous media. If the pore phase is continuous from one end to the other in one direction of the 3D digital coal, it means that the digital coal is connected in that direction. Digital coal is composed of a large number of discrete pixels, and the connectivity between pixels can be described in three ways: 6-connected (i.e., voxels with a common face are said to be connected), 18-connected (i.e., voxels with at least one common edge are said to be connected) and 26-connected (i.e., voxels with at least one common vertex are said to be connected; Fig. 6; Zhang et al., 2018; Wang et al., 2020; Fang et al., 2021).

In this study, the connectivity analysis was mainly carried out by means of 6-connected processing, that is, voxels with common faces were considered to be connected (Fig. 6a). The reservoir porosity and connected porosity can be respectively calculated according to Eqs. (1)-(2):

$$\varphi = \frac{V_p}{V_c} \tag{1}$$

$$\varphi_c = \frac{V_{c-p}}{V_c} \tag{2}$$

where, φ and φ_c respectively represent reservoir porosity and connected porosity, V_p and V_{c-p} respectively represent pore volume and connected pore volume, and the V_c characterizes the analytical volume of digital sample.
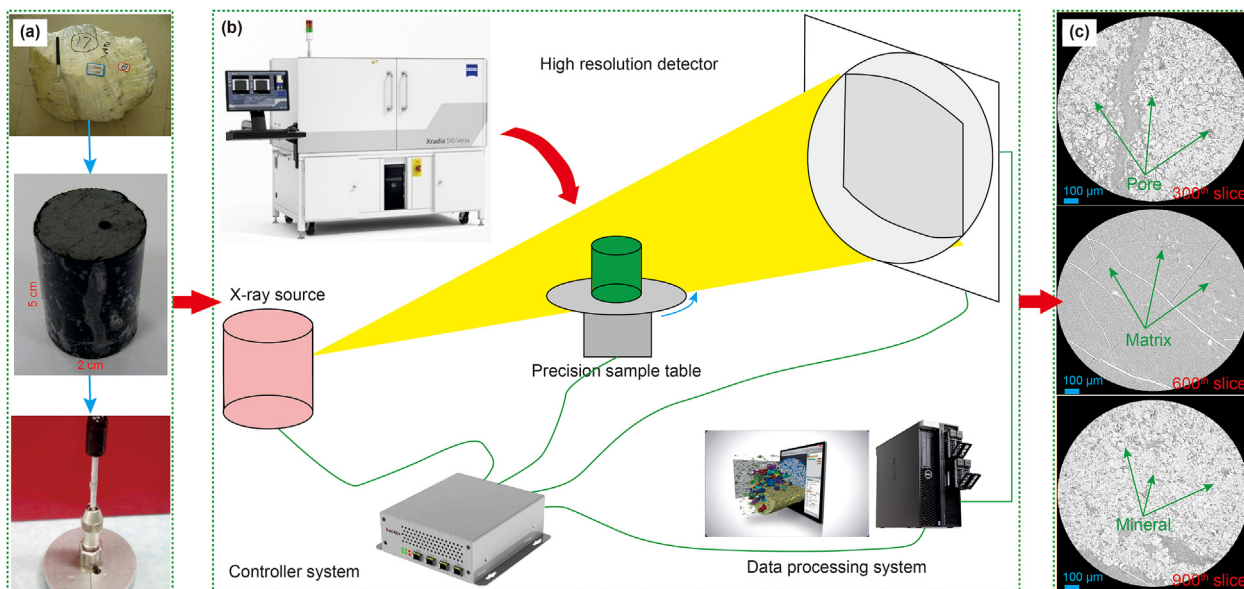
Fig. 2. The X-ray CT scanning system using the YW sample as an example. (a) Preparation of sample; (b) Imaging system components; (c) Typical 2D CT slices of YW sample.

Table 2
Dimensions of two coal samples used in this study.

Sample ID	Sample shape	Number of voxel	Voxel size
SH	Cylindrical type	$988 \times 1013 \times 990$	1.00 μm
YW	Cylindrical type	$988 \times 1014 \times 990$	1.00 μm

2.5. Calculation of fractural dimension in digital coal

The box-counting dimension method is one of the most commonly used methods to calculate the fractal dimension of pore/fracture networks in digital image (Wu et al., 2019a, 2019b), which can be characterized by Eq. (3):

$$D_{f,2D/3D} = \lim_{r \to 0} \frac{\log[N(r)]}{-\log(r)} \qquad (3)$$

where D_f is the fractal dimension; $N(r)$ is the number of boxes (i.e.,

sub-cubes) covering the 3D cubes; and r is the side length of the sub-cube, which can be calculated by dichotomy (He et al., 2021), and the calculation formula can be shown as follows:

$$\delta_k = \frac{1}{r^{k-1}} \left| 0 < k \le \left| \frac{\log \min(x,y,z)}{\log r} \right| + 1 \right. (k = 0, 1, 2, 3 \dots\dots) \qquad (4)$$

where, x, y and z respectively represent the side lengths of the sub-cubes divided.

Fig. 7 is a schematic diagram of calculating fractal dimension by using box-counting dimension method: (1) Determine the side length r of box; (2) Cover and segment the digital coal image after binarization process with boxes of different scales; (3) Cumulatively calculate the number of cubes $N(r)$ covering the pore/fracture space; (4) The set of $(r, N(r))$ can be obtained by changing the side length r of the sub-cube; (5) Perform linear fitting between log $[N(r)]$ and $-\log(r)$, and the slope of the fitting curve is the fractal dimension (Fig. 7).
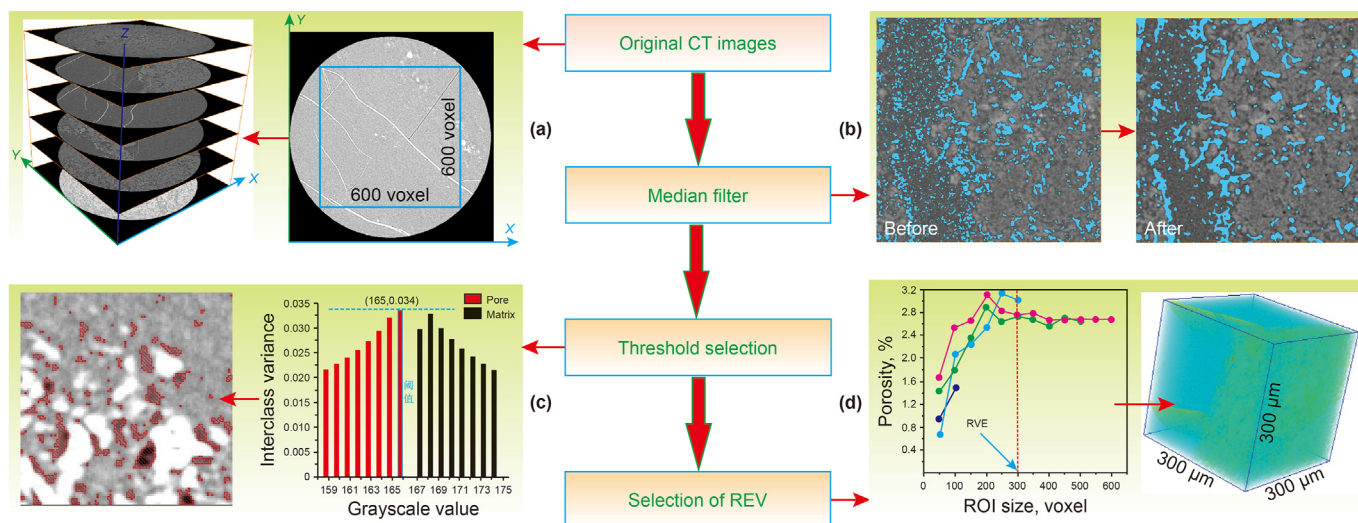

Fig. 3. Image processing flow diagram using the SH sample as an example. (a) Original CT section; (b) Median filtering processing; (c) Threshold selection; and (d) Selection of REV.
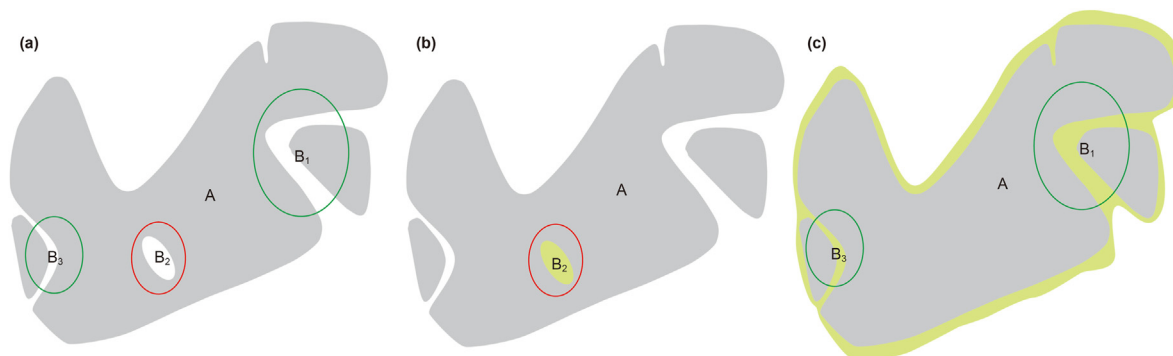
Fig. 4. Numerical simulation of matrix swelling process. (a) Original image; (b) Swelling image with the pore B_2 in matrix; and (c) Swelling image with B_1 and B_3 regions at the edge of the matrix.

Table 3
Threshold range of pores/fractures of SH and YW samples under different matrix swelling contents.

Sample ID	Threshold range of pores/fractures	Threshold segmentation range of pores/fractures					
		0.00%	0.30%	0.60%	0.90%	1.20%	1.50%
SH	−31744/−9767	−31744/−9767	−31744/−9773	−31744/−9779	−31744/−9785	−31744/−9793	−31744/−9799
YW	−32512/−22467	−32512/−22467	−32512/−22469	−32512/−22472	−32512/−22474	−32512/−22476	−32512/−22478

Select representative elementary volume

Extract pores and fractures and calculate porosity

Calculate porosity under corresponding matrix swelling

Re-determine the corresponding thresholds for each porosity

Extract the pores and fractures again and analyze its connectivity

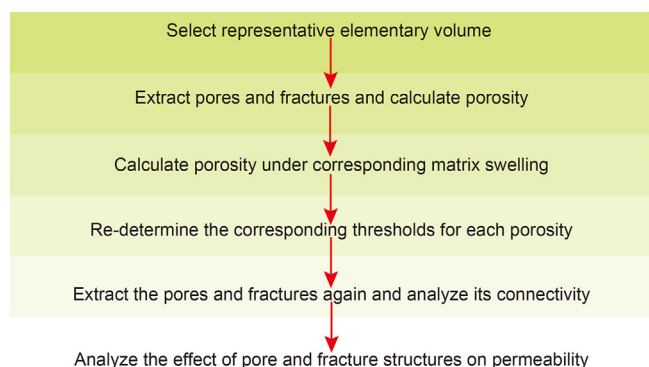Analyze the effect of pore and fracture structures on permeability

Fig. 5. Schematic operation flow of matrix swelling.

2.6. Calculation of absolute permeability in digital coal

This study mainly explores the pore/fracture structure of coal reservoir and its corresponding changes of permeability under different matrix swelling contents. The analyzed samples require effective interconnected pores/fractures to provide corresponding seepage channels. Therefore, the connectivity analysis of two samples should be required and the isolated pores/fractures should be removed (Fig. 8).

In this study, it is assumed that the fluid density is constant and there is no slip phenomenon at the boundary. That is, it is thought to be an incompressible viscous flow. The micro-flows can be simulated using Navier-Stokes equations (Zhang et al., 2019b; Wang et al., 2020), and the absolute permeability can be calculated using Darcy's law (Ni et al., 2020; Xie et al., 2020), which are as follows:

$$K = \frac{Q\mu L}{A \cdot \Delta P} = \frac{G}{A} \frac{\mu L}{\rho \cdot \Delta P} \tag{5}$$

where, K is the absolute permeability, m^2; Q is the volume flow, m^3/s; μ is the dynamic viscosity coefficient, Pa·s; L is the fluid flow length, m; A is the cross sectional area of fluid passing through the pore/fracture grid, m^2; ΔP is the pressure difference, Pa; G is the mass flow rate; and ρ is the fluid density.

In this study, the inlet and outlet of fluid flow were set as two opposite surfaces, the pressure constraint was set as the boundary
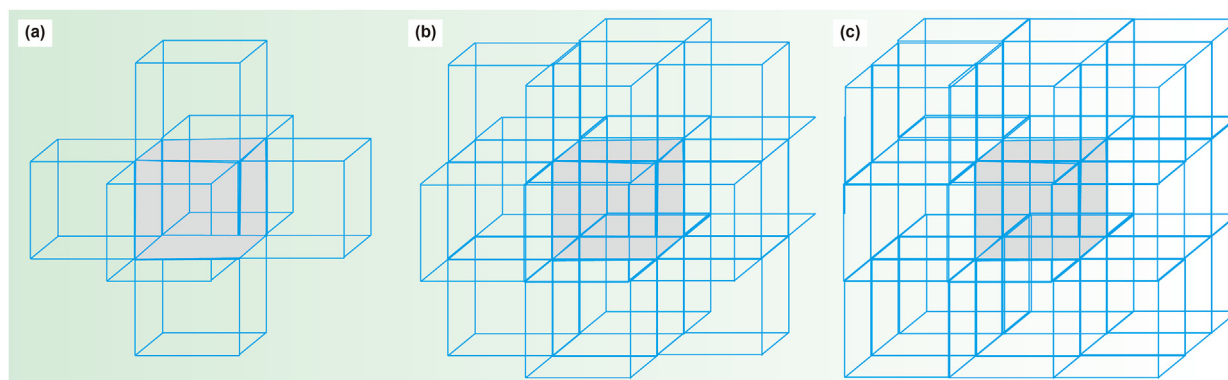

Fig. 6. Schematic diagram of extraction of minerals touched by interconnected pores and fractures. (a) 6-connectivity; (b) 18-connectivity; (c) 26-connectivity.
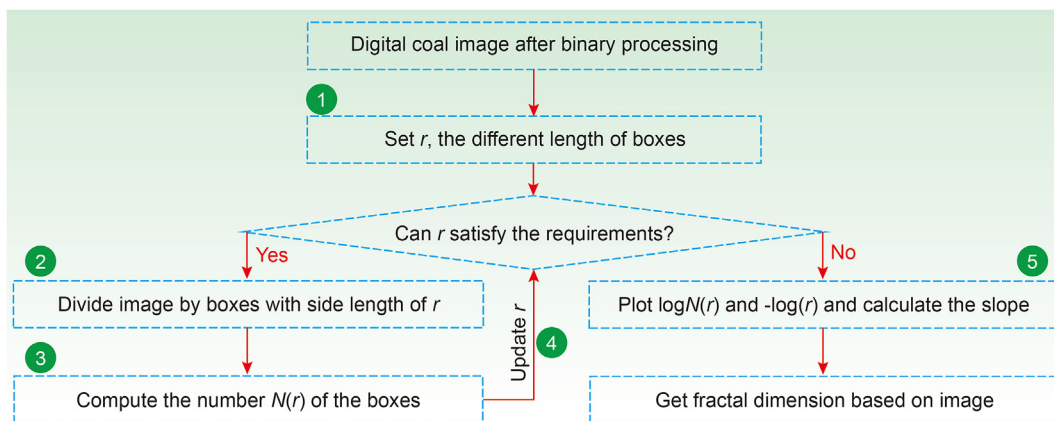
Fig. 7. Schematic diagram of fractal dimension calculation based on the digital coal images.
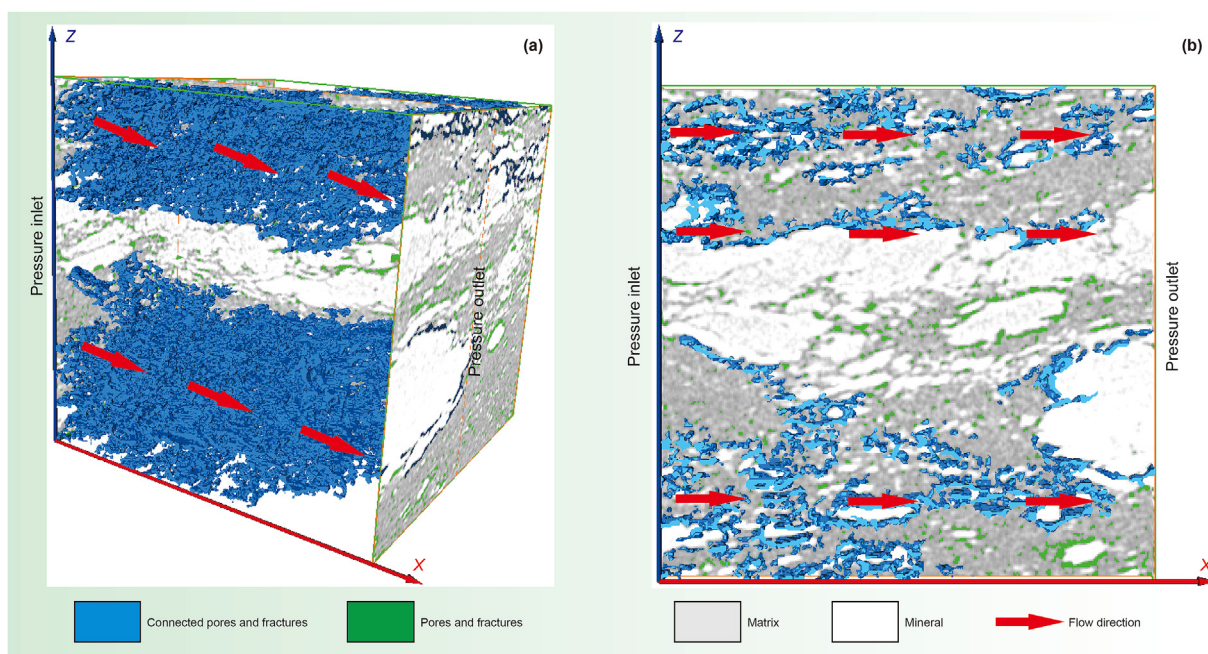

Fig. 8. Schematic diagram of boundary condition setting using the X direction in YW sample as an example. (a) Three-dimensional view; and (b) Two-dimensional view.

conditions of the inlet and outlet, and the boundary conditions of the other four surfaces were set as the no-slip surface. The inlet pressure was 0.13×10^{-6} MPa, the outlet pressure was 0.10×10^{-6} MPa, and the dynamic viscosity of water was 0.001 Pa·s, and the density of water is equal to 1000 kg/m^3 (Fig. 8).

3. Results

3.1. Microstructure characteristics and segmented phases of digital coal

In order to intuitively explore the influence of matrix on pore/fracture structure, the FIB-SEM technology was used to scan the region of interest in the analysis domain with nano-scale resolution, and its typical 2D slices can be shown in Fig. 9. The black, gray and white in typical 2D slices represent pores/fractures, matrixes and minerals, respectively, which indicates the microstructure of the reservoir is highly heterogeneous (Fig. 9). The pores/fractures are often filled with minerals, which will make the permeability

worse. There are intra-matrix pores (i.e., the pores are developed within the matrix), matrix-edge fractures (i.e., the fractures are developed at the edge of the matrix) and intra-mineral pores (i.e., the pores are developed within the mineral) in coal reservoir, among which, the intra-matrix pores and matrix-edge fractures are the focus of this study, and the contacting area between matrix and pores/fractures is the core area of matrix swelling (Fig. 9).

The pore/fracture, matrix and mineral can be respectively extracted from REV, and the connected pores/fractures can be further extracted from pores/fractures (Fig. 10). The gray area represents the pores, which are ellipsoidal and conical in each region of the sample space. Blue area is inorganic mineral, which is mainly distributed in the middle of sample space with irregular shape. Green area represents the matrix, which is a kind of organic matter that accounts for a large proportion of coal (Fig. 10). The interconnected pores/fractures in SH sample are mainly distributed in sheets, while those in YW sample are mainly distributed in bands (Fig. 10). The spatial distribution of the interconnected pores/fractures has a great influence on the permeability evolution, and the
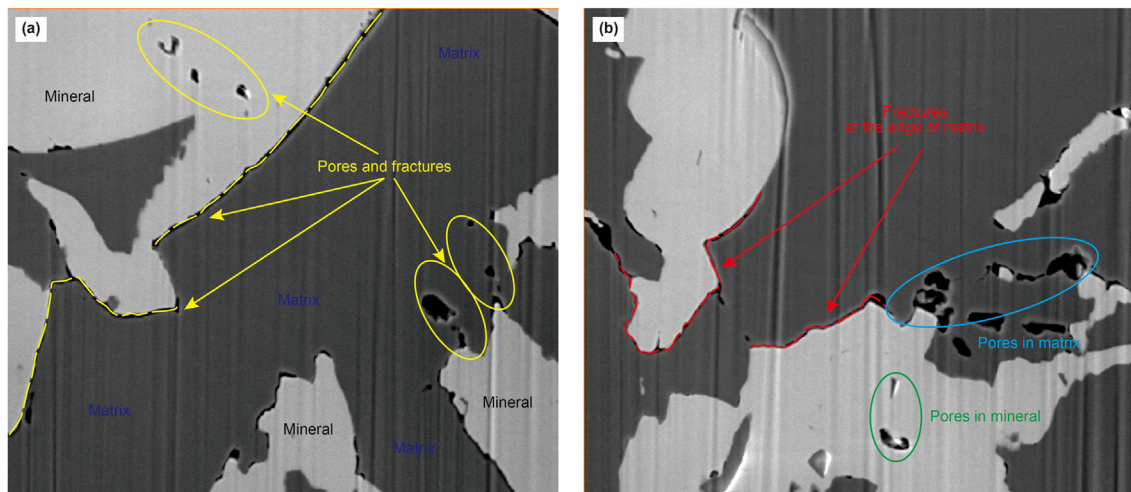
Fig. 9. Microstructure characteristics of coal reservoir. (a) Distribution of pore, matrix and mineral phases in coal reservoir, and (b) Pores and fractures distribution in mineral and matrix phases.

transformation and reconstruction of the interconnected pores/fractures by the swelling effect is the core content of this study. The visualization and reconstruction results of SH and YW samples show that the reservoir structure has high spatial heterogeneity.

Calculate the volume fraction of each component in REV, and the calculation results are shown in Table 4. For SH sample, the volume fraction of pores/fractures, matrixes and minerals are 10.823%, 83.024% and 6.153%, respectively. For YW sample, the volume fraction of pores/fractures, matrixes and minerals are 8.059%, 58.780% and 33.161%, respectively (Table 4). The porosity of the interconnected pores in SH and YW samples is 3.33% and 5.44% respectively, which indicates that the coal samples have good connectivity. The 3D fractal dimension is between 2 and 3, and the higher the fractal dimension is, the more complex the pore/fracture structure is. The fractal dimension of the interconnected pores/fractures of SH and YW samples is 2.27 and 2.18 respectively, which indicates that the structures of the interconnected pores/fractures in coal samples are simple.

3.2. 3D visualization of matrix phase under different particle sizes

This study mainly discusses the influence of matrix swelling on the interconnected pore/fracture structures. Therefore, it is necessary to further analyze the matrix phase in digital coal. In this study, the matrix phase in digital coal is regarded as equivalent particles, and the size, area, volume and other parameters can be analyzed according to the size of the particles, and then the evolution morphology of the matrix can be evaluated.

In the analytical domain of SH sample, the number of matrix particles is limited, and they are concentrated in the size range of 0−3 μm and >12 μm, and there is no matrix development in other size ranges (Fig. 11a). When the size of matrix particles is less than 12 μm, the matrix development is usually isolated (Fig. 11a). When the size of matrix particles is larger than 12 μm, the matrix development shows a connected distribution, and the swelling effect of this matrix part has a great influence on the reconstruction of the interconnected pore/fracture structures (Fig. 11a). When the size of matrix particles is 0−3 μm, the mean values of equivalent radius, length, width, area and volume are 1.41 μm, 1.68 μm, 1.30 μm, 4.54 μm^2 and 4.58 μm^3, respectively (Table 5). When the size of matrix particles is greater than 12 μm (i.e. 349.80 μm), the average length, width, area and volume of matrix particles are

519.07 μm, 328.45 μm, 7490870 μm^2 and 22411200 μm^3, respectively (Table 5).

For the matrix phase of YW sample, it is distributed in different size ranges, and the number of particles decreases with the increase of size. In 0−3 μm, 3−6 μm, 6−9 μm, 9−12 μm and >12 μm, the number of particles is 9818, 1165, 50, 7 and 1, respectively (Fig. 11b; Table 5). Similar to SH sample, when the pore size of matrix particles is less than 12 μm, the development of matrix usually presents an isolated distribution (Fig. 11b). When the size of matrix particles is larger than 12 μm, the matrix development shows a connected distribution. The swelling effect of matrix in this part has a great influence on the interconnected pore/fracture structures, which is the key part of the matrix phase in this study (Fig. 11b). With the increase of particle diameter, the average value of equivalent radius, length, width, area and volume all increase. When the diameter of matrix particles is 311.16 μm, the average length, width, area and volume of matrix particles are 519.07 μm, 328.45 μm, 6548020 μm^2 and 15773900 μm^3, respectively (Fig. 11b; Table 5).

4. Discussion

4.1. Microstructure evolution of pores and fractures due to matrix swelling

Fig. 12 shows the microstructure evolution of the interconnected pores/fractures in SH and YW samples under different swelling contents. The different colors in Fig. 12 respectively represent different pores/fractures. Although there are a large number of pores/fractures in the analysis domain, the distribution of interconnected pores/fractures is limited, and only 2 connected pores/fractures are distributed in sample (Fig. 12). The change of the characterizing color for same pores/fractures under different swelling contents reflects the influence of swelling effect on the pore/fracture structures. In SH sample, the pores/fractures are only connected in the Z direction (Fig. 12b), while in YW sample, which are only connected in the X and Y directions (Fig. 12d). Although there is little difference between the visualization results of interconnected pores/fractures under different swelling contents (Fig. 12), the influence of swelling on reservoir microstructure can be quantitatively analyzed through the change of geometric parameters of pore/fracture structures (Figs. 13−14).
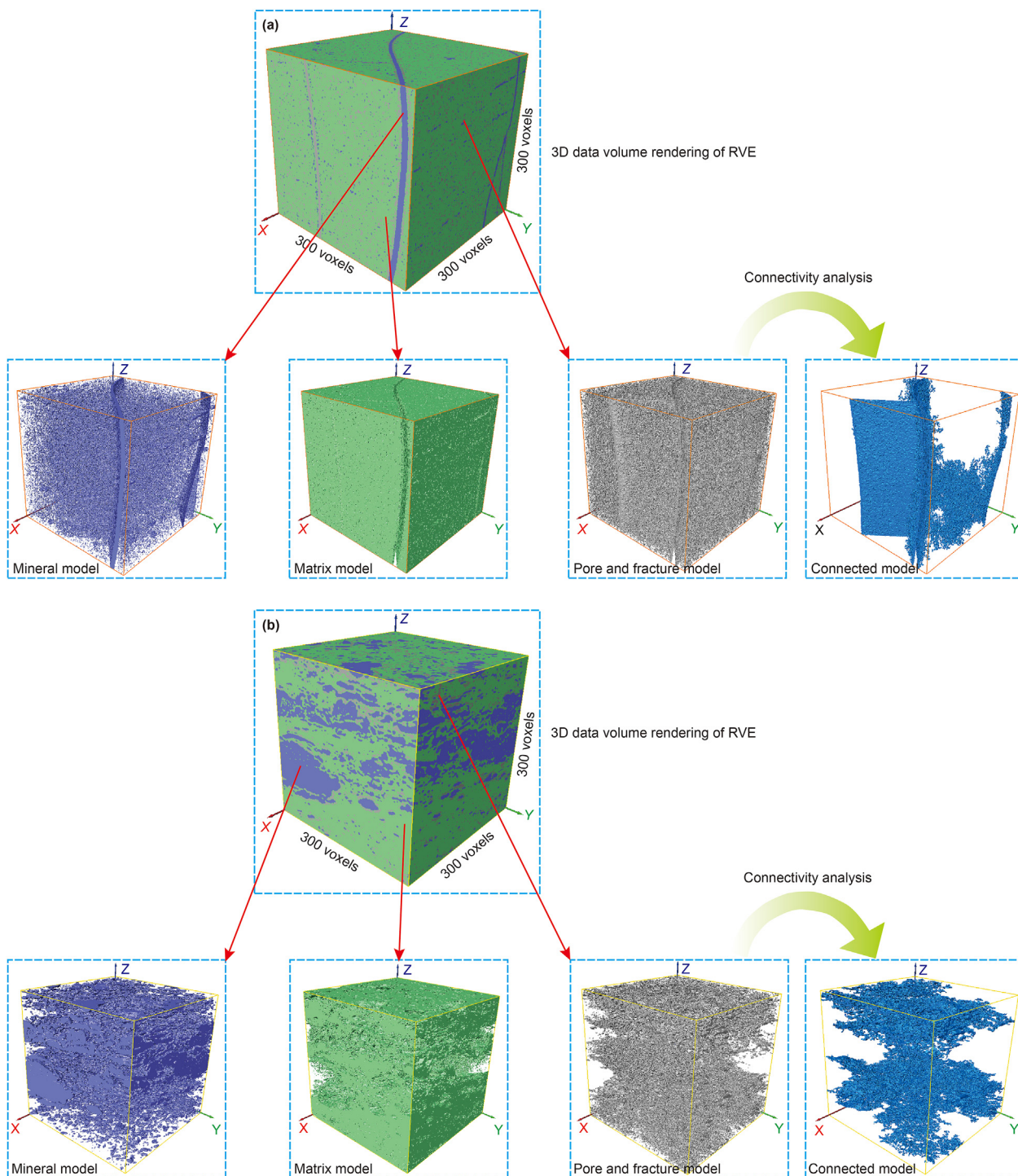
Fig. 10. 3D visualization characterization of coal reservoir structure model and its connectivity analysis. (a) SH sample; (b) YW sample.

Table 4
Calculation results of coal sample component content.

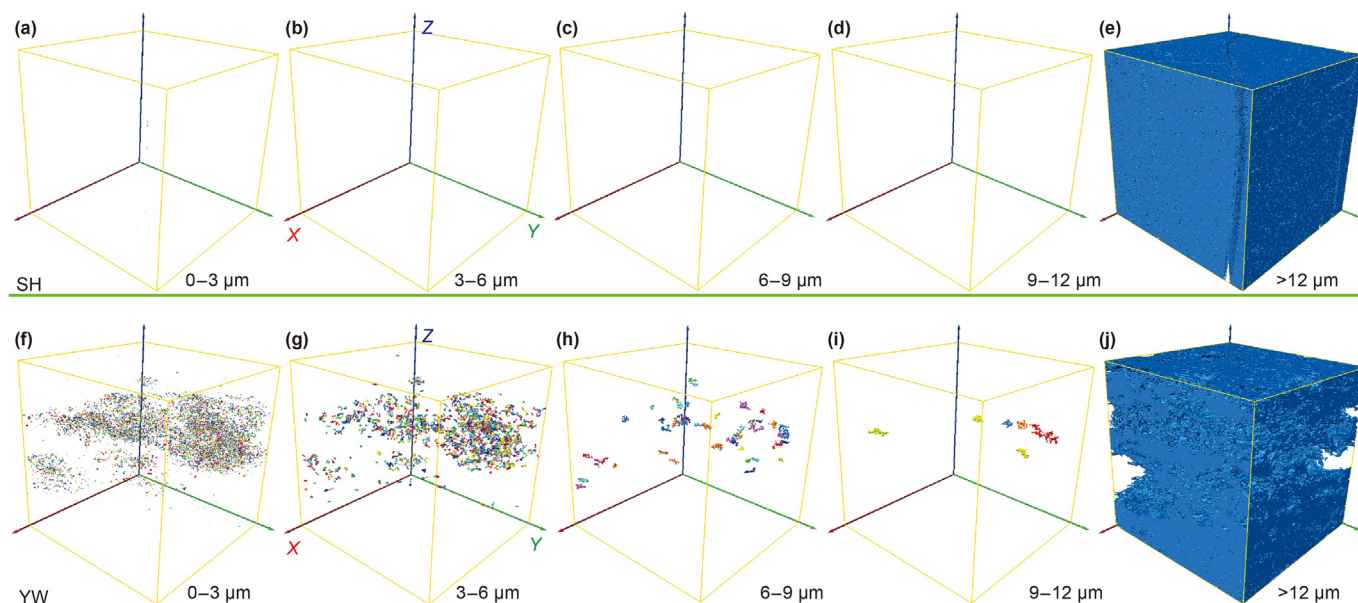| Sample ID	Pore model			Matrix model			Mineral model		
	Voxel count	Volume, μm³	Volume fraction, %	Voxel count	Volume, μm³	Volume fraction, %	Voxel count	Volume, μm³	Volume fraction, %
SH	2.92×10^6	2.92×10^6	10.823	2.24×10^7	2.24×10^7	83.024	1.66×10^6	1.66×10^6	6.153
YW	2.18×10^6	2.18×10^6	8.059	1.59×10^7	1.59×10^7	58.780	8.97×10^6	8.97×10^6	33.161

Fig. 11. Results of X-ray CT data analysis showing 3D visualization of matrix phase under different scales. (a—e) SH sample; (f—j) YW sample.

Table 5
Results of parameter calculation of matrix phase under different scales.

Samples	Parameters	Particle sizes, μm				
		0—3	3—6	6—9	9—12	>12
SH	Number	12	0	0	0	1
	Diameter, μm	(1.24—1.79)/1.41	—	—	—	(349.80—349.80)/349.80
	Length, μm	(1.09—3.08)/1.68	—	—	—	(519.07—519.07)/519.07
	Width, μm	(1.09—1.63)/1.30	—	—	—	(328.45—328.45)/328.45
	Area, μm²	(3.00—8.28)/4.54	—	—	—	(7490870-7490870)/7490870
	Volume, μm³	(1.00—3.00)/1.58	—	—	—	(22411200-22411200)/22411200
YW	Number	9818	1165	50	7	1
	Diameter, μm	(1.24—2.99)/1.73	(3.06—6.00)/3.78	(6.02—8.85)/6.84	(9.18—11.02)/9.81	(311.16—311.16)/311.16
	Length, μm	(1.09—7.87)/2.63	(4.49—21.60)/8.39	(10.58—28.45)/18.99	(23.34—37.39)/29.73	(519.07—519.07)/519.07
	Width, μm	(1.09—4.03)/1.62	(3.35—8.72)/4.12	(6.10—14.51)/9.19	(12.60—17.20)/14.79	(328.45—328.45)/328.45
	Area, μm²	(3.00—35.65)/8.69	(27.88—223.58)/61.16	(157.35—644.15)/303.21	(644.21—1248.63)/874.60	(6548020-6548020)/6548020
	Volume, μm³	(1.00—14.00)/3.43	(15.00—113.00)/31.00	(114.00—363.00)/174.00	(405.00—700.00)/499.29	(15773900-15773900)/15773900

Notes: (Minimum value—Maximum value)/Average value.

Fig. 13 shows the parameter changes of pores/fractures structures under different swelling contents. With the increase of swelling content, the number of pores/fractures decreases. The number of pores/fractures in SH sample changes evenly, while which significantly changes at a lower level and gently at a higher level in YW sample (Fig. 13a). The porosity of SH and YW samples decreases from 10.9% and 8.08% to 10.63% and 7.81%, respectively. The porosity shows a decreasing trend, and the variation trend between samples was relatively consistent (Fig. 13b). The fractal dimension of SH and YW samples decreases from 2.4832 and 2.3780 to 2.4822 and 2.3723, respectively. The decreasing trend of the fractal dimension between samples indicates that the increase of the swelling content made the development of pores/fractures simpler and its complexity gradually decreased (Fig. 13c). The pore width of SH and YW samples decreases from 2.4799 μm and 2.24699 μm to 2.4722 μm and 2.24399 μm, respectively. The decreasing trend of width between samples indicates that with the increase of swelling content, the spacing between samples became narrower and narrower, which shows that the swelling effect has a great influence on the development of pore/fracture structures (Fig. 13d). The surface area and volume of pores/fractures also decrease in accordance with the above structural parameters. The

surface area of SH and YW samples decreases from 51.70 μm² and 87.697 μm² to 49.07 μm² and 84.912 μm², respectively (Fig. 13e). The volume decreases from 28.23 μm³ and 62.362 μm³ to 26.69 μm³ and 60.0417 μm³ (Fig. 13f). The variation of structural parameters under different swelling contents indicates that the matrix swelling has an effect on the microstructures of coal reservoir.

Fig. 14 shows the variation of structural parameters of connected pores/fractures in reservoir under different swelling contents. With the increase of swelling content, the number of connected pores/fractures did not change (Fig. 14a), which mainly because there were only two connected fractures in SH and YW samples, and the reconstruction effect of swelling effect on pore/fracture microstructures was weak in connected pores/fractures. The porosity of SH and YW samples decreases from 5.44% and 3.33% to 5.16% and 3.04% respectively (Fig. 14b), and the decrease of porosity of connected pores/fractures led to poor connectivity of samples, which will be bound to have a negative impact on fluid migration in the process of CO_2-ECBM. The fractal dimension of SH and YW samples decreases from 2.180 and 2.269 to 2.145 and 2.258, respectively (Fig. 14c), which indicates that the morphological development of connected pores/fractures is relatively simple and its spatial
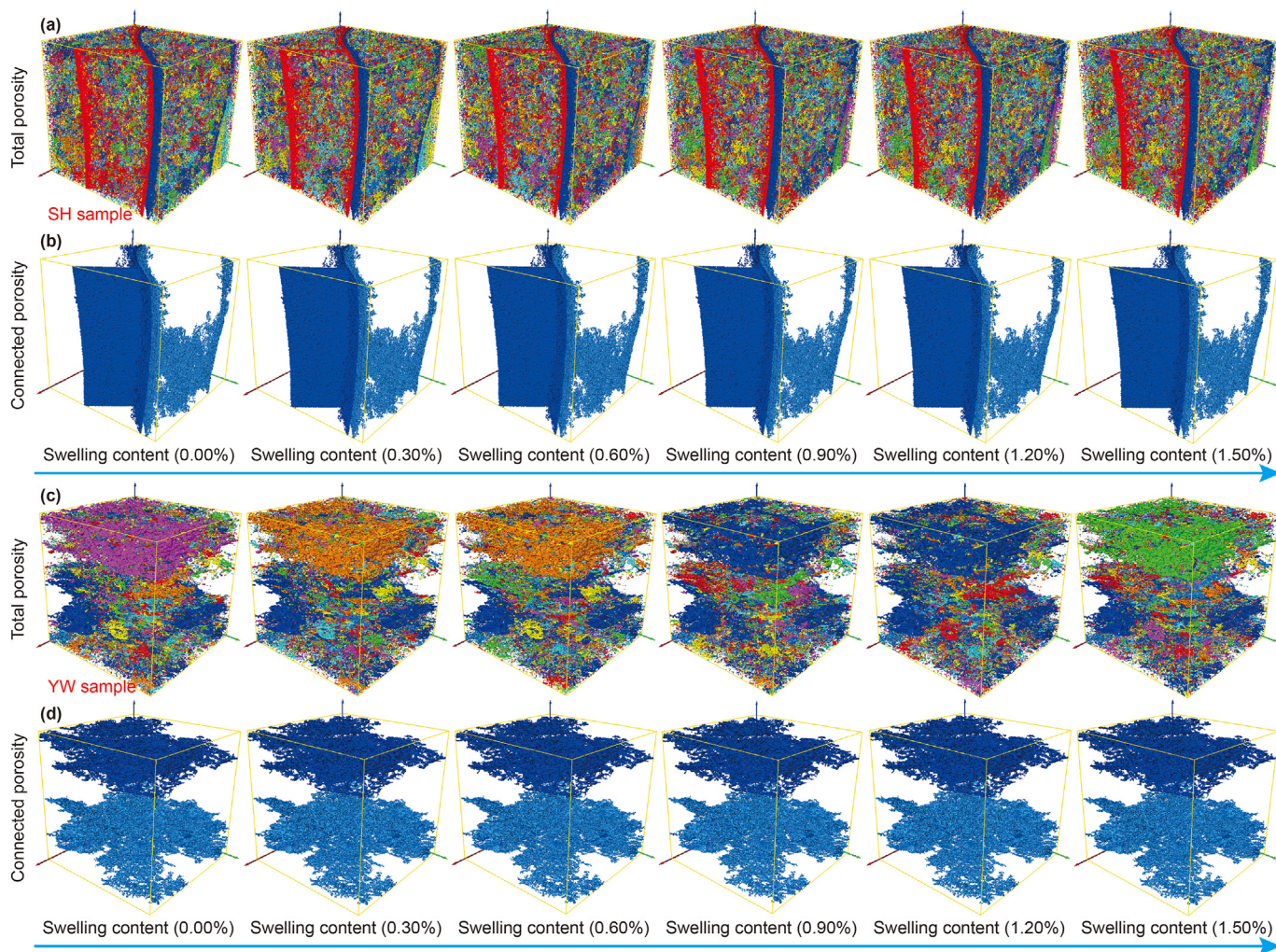
Fig. 12. Microstructure evolution under different matrix swelling contents. (a–b) SH sample; (c–d) YW sample; (a/c) Total porosity; and (b/d) Connected porosity.
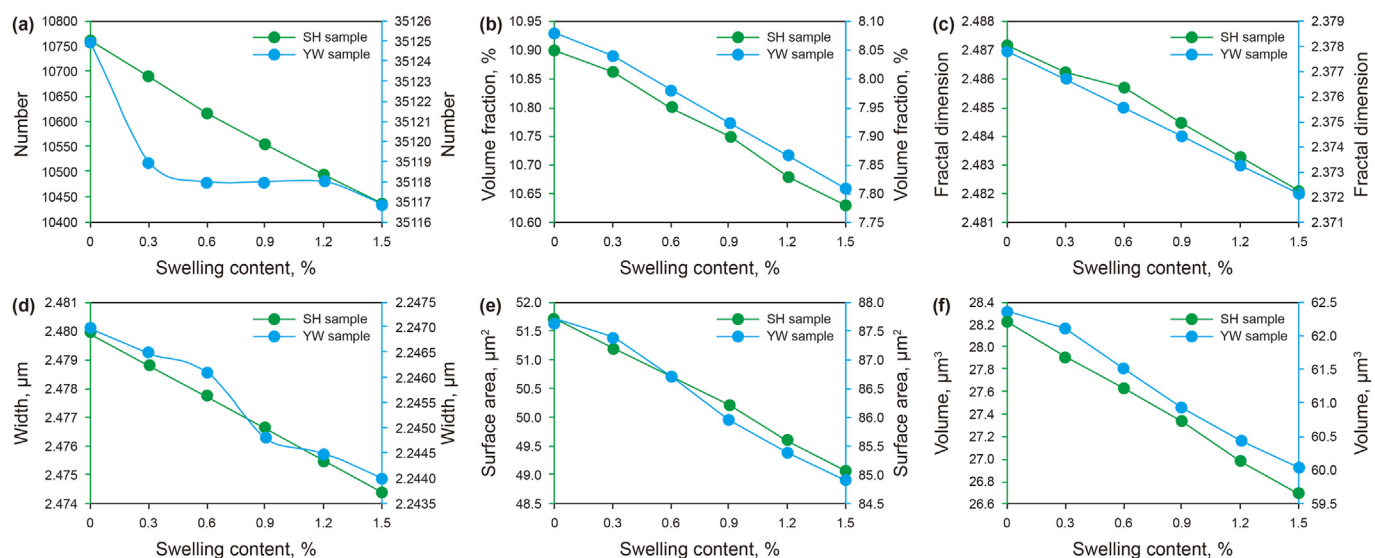

Fig. 13. Parameter evolution of pores/fractures under different matrix swelling contents. (a) Number; (b) Volume fraction; (c) Fractal dimension; (d) Width; (e) Surface area; and (f) Volume.
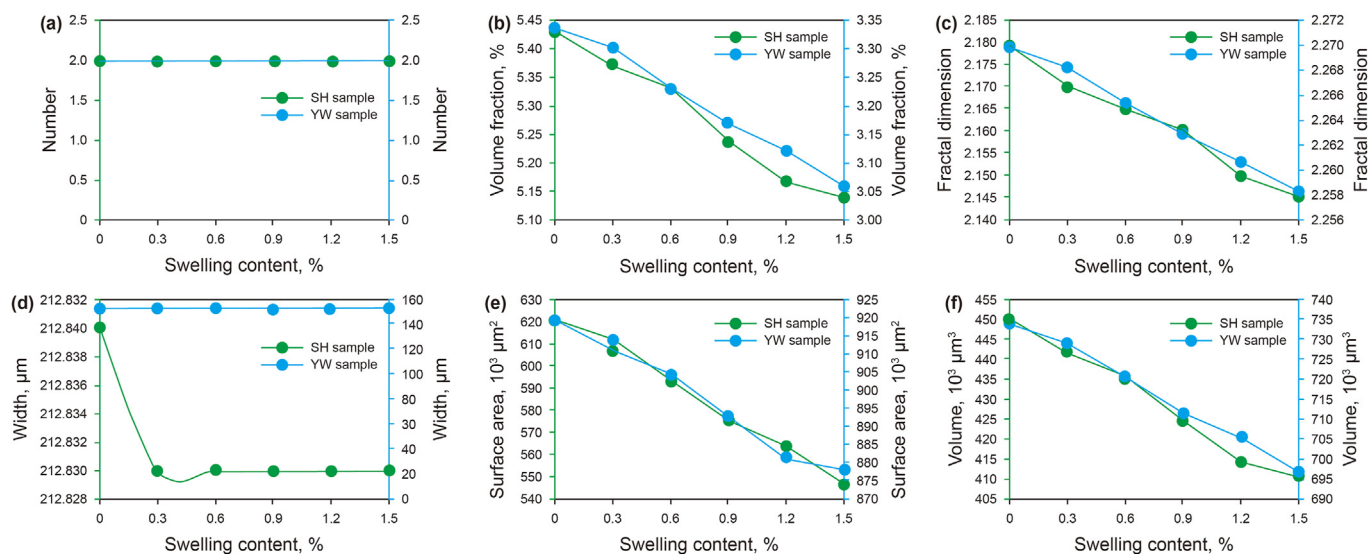
Fig. 14. Parameter evolution of interconnected pores/fractures under different matrix swelling contents. (a) Number; (b) Volume fraction; (c) Fractal dimension; (d) Width; (e) Surface area; and (f) Volume.

complexity is low, which also indicates the influence of matrix swelling on the reconstruction of connected pores/fractures is weaker than that of non-connected pores/fractures. The widths of connected pores/fractures of SH and YW samples remains at 212.832 μm and 151.873 μm, respectively (Fig. 14d), which indicates that matrix swelling effect has almost no influence on the widths of connected pores/fractures. The surface area of SH and YW samples decreases from 919308.8 μm^2 and 621451.5 μm^2 to 873969.5 μm^2 and 552877.9 μm^2, respectively (Fig. 14e). The volume decreases from 733930.5 μm^3 and 449787.5 μm^3 to 696687.0 μm^3 and 410939.5 μm^3, respectively (Fig. 14f). The changes of structural parameters of connected pores/fractures under different matrix swelling contents indicate that the matrix swelling will affect the microstructure changes of interconnected pores/fractures, and further affect the fluid migration during CO_2-ECBM process.

Fig. 15 shows the variation range of structural parameters of pores/fractures in coal reservoir under different matrix swelling contents. When the swelling content increases from 0.30% to 0.60%, and 0.90% to 1.20%, the variation range of structural parameters increases. When the swelling content increases from 0.60% to 0.90%, and 1.20% to 1.50%, the variation range of each structural parameter shows a decreasing trend. Therefore, with the increase of swelling content, the variation range of structural parameters of pores/fractures in digital coal increases first and then decreases. The number and width of interconnected pores/fractures are almost not affected by the matrix swelling content. The variation range of volume fraction and fractal dimension is consistent between different samples (Fig. 15).

4.2. Effects of matrix swelling on reservoir permeability

In order to investigate the influence of different swelling contents on permeability evolution, the numerical simulation of single-phase fluid was carried out using the connected pores/fractures as geological carrier. In this numerical simulation study, it is assumed that the contacting surface of fluid and solid is non-slip surface, and the interconnected pores/fractures are separated from the matrix. In this study, the analysis domain was 300 × 300 × 300 pixels, and its actual voxel was 300 × 300 × 300 μm^3. The maximum interconnected pores/fractures was firstly extracted in the analysis domain.

The absolute permeability in reservoir is calculated under different matrix swelling contents, and the quantitative results are shown in Table 6. During the simulation process of matrix swelling effect, the absolute permeability of SH and YW samples decreases from 19.122 mD to 18.696 mD and 20.618 mD to 19.522 mD, respectively. The negative contribution of matrix swelling effect to absolute permeability of SH and YW samples increases from 0.368% to 0.633% and 0.868% to 1.404%, respectively, and the net contribution is 0.265% and 0.836% (Table 6). The absolute permeability of samples decreases with the increase of matrix swelling effect, which indicates that matrix swelling can reduce the fluid flow capacity in reservoir, which is bound to negatively affect the transport of CO_2 and CH_4 in the process of CO_2-ECBM.

The evolution of fluid velocity field under different matrix swelling contents is shown in Fig. 15. The flow direction of SH and YW samples is X and Z axis respectively, which is consistent with this direction. The density of streamlines decreases with the increase of matrix swelling, and the fewer routes through which the fluid flows, the lower its permeability (Fig. 16b and 16d). For SH and YW samples, the difference of streamline density is small under different swelling contents, which also indicates that the change of absolute permeability is small, and the single swelling effect has a limited influence on permeability. The interconnected fractures of YW sample are more developed than that of SH sample (Fig. 16a and 16c), and the interconnected fractures have a greater impact on permeability, which also well explains that the absolute permeability of YW sample is higher than that of SH sample, and the negative contribution of matrix swelling effect to YW sample is greater than that of SH sample.

4.3. Mechanism analysis of permeability evolution during CO_2-ECBM process with matrix swelling effect

In the process of CO_2-ECBM, the connected pores/fractures of coal reservoir, as the main channel of fluid migration, are bound to have a negative impact on CO_2 storage and CH_4 stimulation under the influence of matrix swelling effect. As the matrix swelling content increases, the number of pores in matrix gradually decreases and the pore radius becomes shorter (Fig. 17). The matrix continuously expands to the connected pores/fractures, and the width of which gradually shorten (Fig. 17). Under the influence of
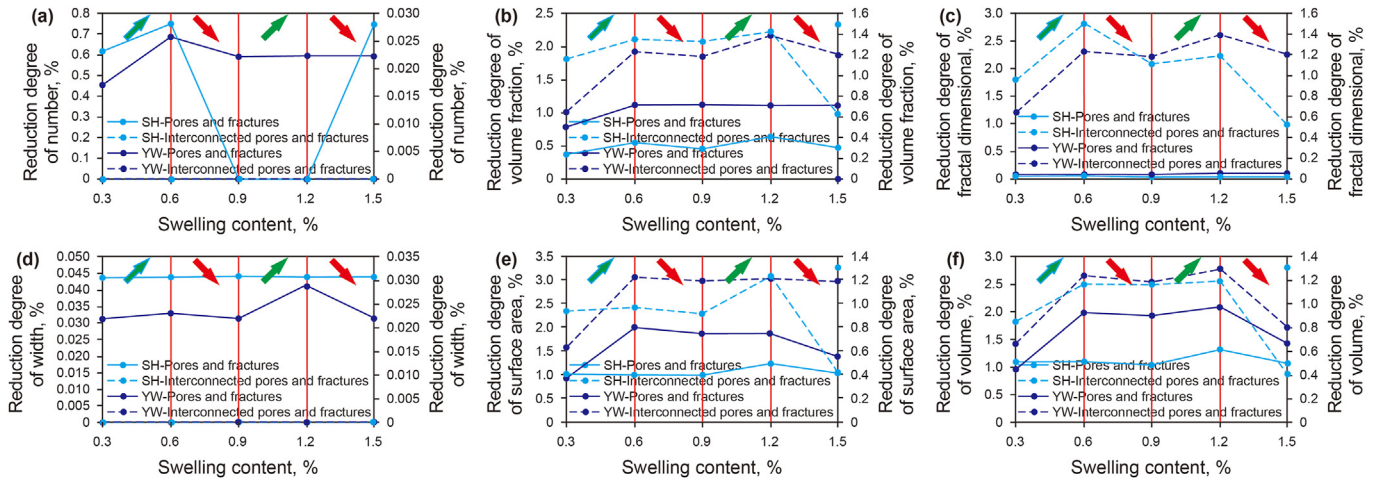
Fig. 15. Reduction degree of parameter of pore/fracture with different swelling contents. (a) Number; (b) Volume fraction; (c) Fractal dimension; (d) Width; (e) Surface area; and (f) Volume.

Table 6
Variation of absolute permeability of SH and HD samples under different swelling contents.

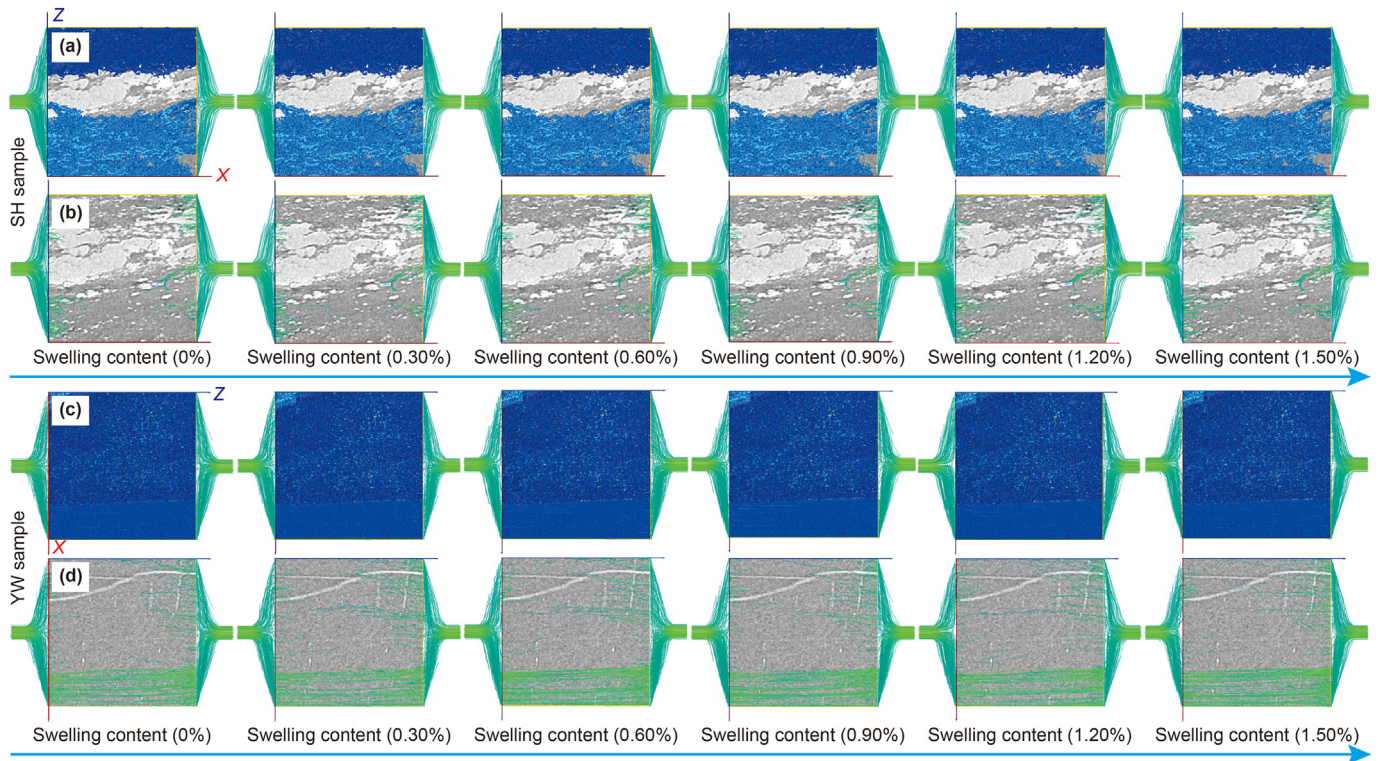| Sample ID	Absolute permeability, mD/Negative contribution degree, %					
	0.00%	0.30%	0.60%	0.90%	1.20%	1.50%
SH	19.122/−	19.001/0.633	18.931/0.368	18.847/0.444	18.736/0.589	18.696/0.213
YW	20.618/−	20.439/0.868	20.152/1.404	19.970/0.903	19.713/1.287	19.522/0.969

Fig. 16. 3D visualization of velocity field of SH and YW samples in the experiment simulation.

matrix swelling on connected pores/fractures, the bending degree of fluid flow increases and the connectivity gradually decreases, so the resistance of fluid migration increases and the permeability decreases gradually.

In the process of CO_2-ECBM, the reservoir permeability is affected not only by matrix swelling caused by competitive adsorption of CH_4 and CO_2, but also by reservoir effective stress effect (Fig. 18). In the area near the gas injection well (i.e. point A in

Fig. 18), the injection of CO_2 will reduce the reservoir effective stress, which will lead to the improvement of porosity and permeability. At the same time, the injected CO_2 will have competitive adsorption with CH_4, and due to the preferential absorption of CO_2 by coal matrix, the injected CO_2 will cause great matrix swelling, which will result in the decrease of permeability. At the same time, the matrix swelling effect caused by the competitive adsorption of CH_4 and CO_2 has a more important influence on permeability than the effective stress effect, and its main importance is increasing (Fig. 18). Therefore, in the process of CO_2-ECBM, the permeability of the area near the CO_2 injection well gradually decreases, and the closer it is to the gas injection well, the permeability decreases. In the area near the production well (i.e. point B in Fig. 18), when the injected CO_2 does not spread to this area, the permeability evolution mechanism is similar to that of the direct exploitation of coalbed methane, which will result in the increase of permeability at the initial stage. When the injected CO_2 began to spread to the area, the permeability evolution mechanism was similar to that of the area near the gas injection well (Fig. 18), which will result in the gradual decrease of permeability in the later stage.

5. Conclusions

Based on the fact that the expansion effect of matrix will affect the pore and fracture structures of coal reservoir and its porosity and permeability, and the core conclusions are as follows:

(1) Pores are usually ellipsoidal and conical and the inorganic minerals are irregular in shape. Interconnected pores/fractures are mainly distributed in sheets and bands, which indicates that reservoir microstructure has high spatial heterogeneity. There are intra-matrix/mineral pores and matrix-edge fractures, among which the intra-matrix pores and matrix-edge fractures are the focus, and the contacting area is the core area of matrix swelling.

(2) The number of matrix particles tends to decrease with the size increase. With the increase of particle diameter, the mean values of radius, length, width, area and volume all increase. When the size is small, the matrix usually presents an isolated distribution, while when the size is large, the matrix presents a connected distribution, and the swelling effect of matrix with larger size has a great influence on the reconstruction of interconnected pores/fractures.

(3) There are many pores/fractures in analysis domain, but the interconnected pores/fractures are limited in distribution and only connected in a certain direction. With the increase of swelling content, the number, porosity, width, fractal dimension, surface area and volume of interconnected pores/fractures decrease, which will influence the microstructure of interconnected pores/fractures, and further affect the fluid migration during the CO_2-ECBM process.

(4) With the increase of swelling content, the negative contribution of swelling to absolute permeability of SH and YW samples increases from 0.368% to 0.633% and 0.868% to 1.404%, respectively. The less the flow route, the density of its streamline gradually decreases, which can reduce the flow capacity. Under different swelling contents, the difference of streamline density is small, which indicates that the change of absolute permeability is small.

(5) During the CO_2-ECBM process, the change of permeability is mainly affected by the matrix swelling effect caused by the competitive adsorption of CH_4 and CO_2. As the matrix swelling content increases, the number of pores in matrix decreases and the pore radius becomes shorter. The matrix continuously expands to the interconnected fractures, and the width of which gradually shorten. Under the influence of the matrix swelling, the bending degree of fluid flow increases and the connectivity gradually decreases, so the
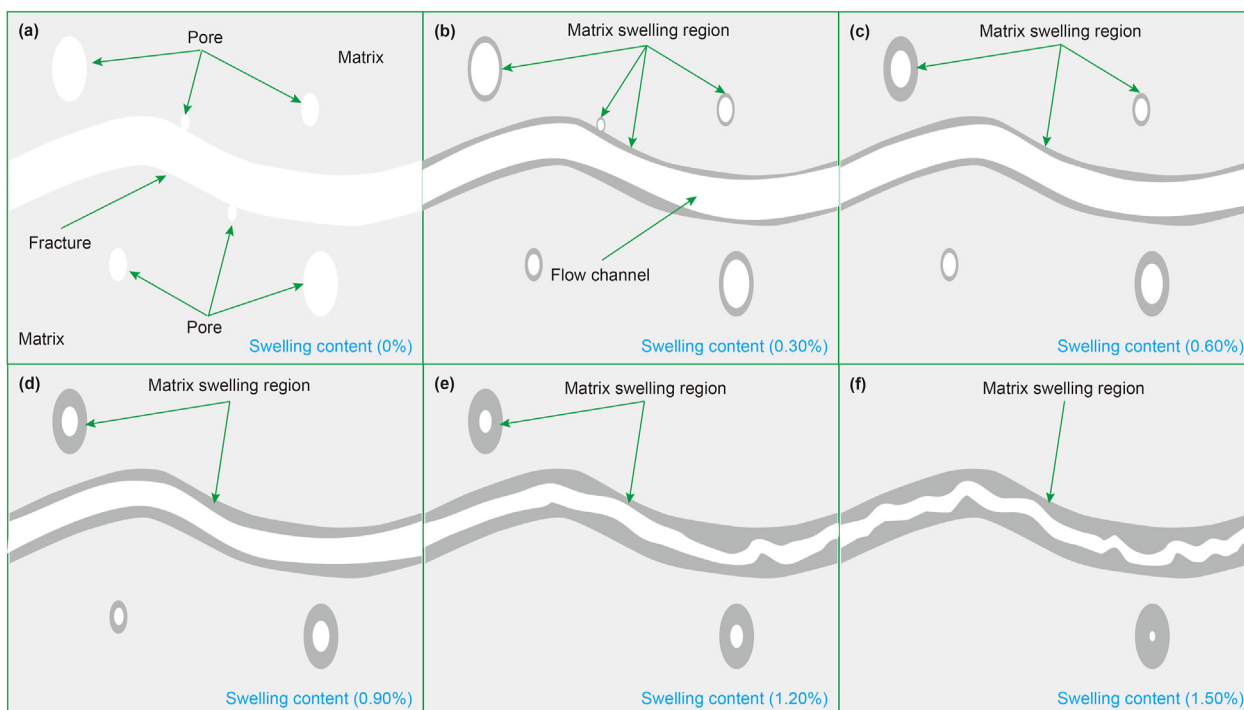

Fig. 17. Schematic diagram of matrix swelling and its effect on microstructure of pore and fracture under different swelling contents.
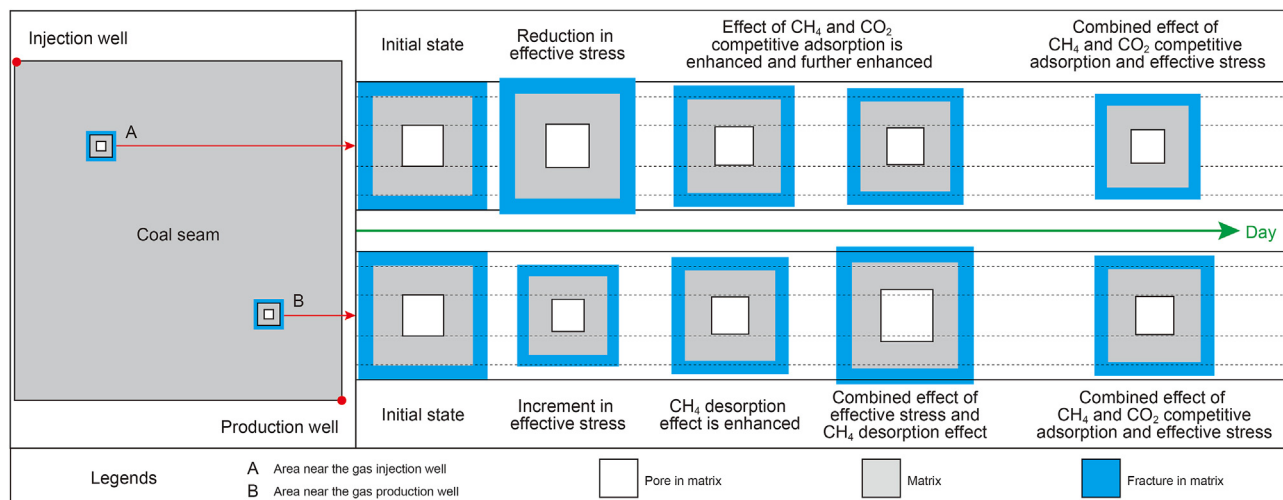
Fig. 18. Schematic diagram of permeability evolution mechanism of CBM reservoir after CO_2 injection.

resistance of fluid migration increases and the reservoir permeability gradually decreases.

References

Bustin, A.M.M., Bustin, R.M., Chikatamarla, L., et al., 2016. Learnings from a failed nitrogen enhanced coalbed methane pilot: Piceance Basin, Colorado. Int. J. Coal Geol. 165, 64—75. https://doi.org/10.1016/j.coal.2016.07.010.

Fang, H.H., Sang, S.X., Liu, S.Q., et al., 2019a. Establishment of dynamic permeability model of coal reservoir and its numerical simulation during the CO_2-ECBM process. J. Petrol. Sci. Eng. 179, 885—898. https://doi.org/10.1016/j.petrol.2019.04.095.

Fang, H.H., Sang, S.X., Liu, S.Q., et al., 2019b. Experimental simulation of replacing and displacing CH_4 by injecting supercritical CO_2 and its geological significance. Int. J. Greenh. Gas Control 81, 115—125. https://doi.org/10.1016/j.ijggc.2018.12.015.

Fang, H.H., Sang, S.X., Liu, S.Q., 2020. Three-dimensional spatial structure of the macro-pores and flow simulation in anthracite coal based on X-ray mu-CT scanning data. Petrol. Sci. 17 (5), 1221—1236. https://doi.org/10.1007/s12182-020-00485-3.

Fang, H.H., Sang, S.X., Du, Y., et al., 2021. Visualization characterization of minerals touched by interconnected pores and fractures and its demineralization effect on coal permeability during CO_2-ECBM process based on X-ray CT data. J. Nat. Gas Sci. Eng. 95, 104213. https://doi.org/10.1016/j.jngse.2021.104213.

Feng, S.B., Wei, Q., Li, X.Q., 2021. Chemical composition variations of altered and unaffected coals from the Huaibei coalfield, China: implications for maturity. Energies 14 (11), 3028. https://doi.org/10.3390/en14113028.

Fujioka, M., Yamaguchi, S., Nako, M., 2010. CO_2-ECBM field tests in the Ishikari coal basin of Japan. Int. J. Coal Geol. 82 (3—4), 287—298. https://doi.org/10.1016/j.coal.2010.01.004.

George, S.J.D., Barakat, M.A., 2001. The change in effective stress associated with shrinkage from gas desorption in coal. Int. J. Coal Geol. 45 (2—3), 105—113. https://doi.org/10.1016/S0166-5162(00)00026-4.

Guo, H., Ni, X.M., Wang, Y.B., et al., 2018. Experimental study of CO_2-water-mineral interactions and their influence on the permeability of coking coal and implications for CO_2-ECBM, 2018 Minerals 8 (3), 117. https://doi.org/10.3390/min8030117.

Hao, D.Y., Tu, S.H., Zhang, C., et al., 2020. Quantitative characterization and three-dimensional reconstruction of bituminous coal fracture development under rock mechanics testing. Fuel 267, 117280. https://doi.org/10.1016/j.fuel.2020.117280.

He, Q., Li, F.X., Shi, A.P., et al., 2021. Fractal characterization of complex hydraulic fracture networks of oil shale via 3D CT reconstruction. Petrol. Geol. Recovery Effic. 28 (5), 116—123 (in Chinese with English abstract.).

Hou, X.W., Liu, S.M., Zhu, Y.M., et al., 2020. Evaluation of gas contents for a multi-seam deep coalbed methane reservoir and their geological controls: in situ direct method versus indirect method. Fuel 265, 116917. https://doi.org/10.1016/j.fuel.2019.116917.

Hu, C.Y., Wang, F.J., Ai, C., 2019. A model of cement-formation interface failure length in supercritical CO_2-ECBM and storage injection well considering the coal swelling effect under high pressure. J. Pet. Explor. Prod. Technol. 9 (4), 2757—2767. https://doi.org/10.1007/s13202-019-0659-0.

Jing, D.J., Meng, X.J., Ge, S.C., et al., 2021. Reconstruction and seepage simulation of a coal pore-fracture network based on CT technology. PLoS One 16 (6), e0252277. https://doi.org/10.1371/journal.pone.0252277.

Long, H., Lin, H.F., Yan, M., et al., 2021. Molecular simulation of the competitive adsorption characteristics of CH_4, CO_2, N_2, and multicomponent gases in coal. Power Technol. 385, 348—356. https://doi.org/10.1016/j.powtec.2021.03.007.

Luo, C.J., Zhang, D.F., Lun, Z.M., et al., 2019. Displacement behaviors of adsorbed coalbed methane on coals by injection of SO_2/CO_2 binary mixture. Fuel 247, 356—367. https://doi.org/10.1016/j.fuel.2019.03.057.

Li, Z.W., Zhang, G.Y., 2019. Fracture segmentation method based on contour evolution and gradient direction consistency in sequence of coal rock CT images. Math. Probl Eng. 2019 (1), 1—8.

Li, Z.B., Wang, F.S., Shu, C.M., 2020a. Damage effects on coal mechanical properties and micro-scale structures during liquid CO_2-ECBM process. J. Nat. Gas Sci. Eng. 83, 103579. https://doi.org/10.1016/j.jngse.2020.103579.

Li, Y.Y., Cui, H.Q., Zhang, P., et al., 2020b. Three-dimensional visualization and quantitative characterization of coal fracture dynamic evolution under uniaxial and triaxial compression based on mu CT scanning. Fuel 262, 116568. https://doi.org/10.1016/j.fuel.2019.116568.

Li, Z., Ni, G.H., Wen, Y.Z., et al., 2021. Analysis of permeability evolution mechanism during CO_2 enhanced coalbed methane recovery based on impact factor method. Fuel 304, 121389. https://doi.org/10.1016/j.fuel.2021.121389.

Liang, Y.T., Tian, F.C., Guo, B.L., et al., 2021. Experimental investigation on micro-structure evolution and spontaneous combustion properties of aerobic heated coal. Fuel 306, 121766. https://doi.org/10.1016/j.fuel.2021.121766.

Liu, S.Q., Sang, S.X., Wang, G., et al., 2017. FIB-SEM and X-ray CT characterization of interconnected pores in high-rank coal formed from regional metamorphism. J. Pet. Sci. Eng. 148, 21—31. https://doi.org/10.1016/j.petrol.2016.10.006.

Majewska, Z., Zietek, J., 2007. Changes of acoustic emission and strain in hard coal during gas sorption-desorption cycles. Int. J. Coal Geol. 70 (4), 305—312. https://doi.org/10.1016/j.coal.2006.07.001.

Ni, X.M., Miao, J., Lv, R.S., et al., 2017. Quantitative 3D spatial characterization and flow simulation of coal macropores based on mu-CT technology. Fuel 200, 199—207. https://doi.org/10.1016/j.fuel.2017.03.068.

Ni, X.M., Zhao, Z., Wang, Y.B., et al., 2020. Optimisation and application of well types for ground development of coalbed methane from no. 3 coal seam in Shizhuang south block in Qinshui basin, Shanxi province, China. J. Petrol. Sci. Eng. 193, 107453. https://doi.org/10.1016/j.petrol.2020.107453.

Sun, Y.F., Zhao, Y.X., Yuan, L., 2018. CO_2-ECBM in coal nanostructure: modelling and simulation. J. Nat. Gas Sci. Eng. 54, 202—215. https://doi.org/10.1016/j.jngse.2018.04.007.

Wang, G., Jiang, C.B., Shen, J.N., et al., 2019. Deformation and water transport behaviors study of heterogenous coal using CT-based 3D simulation. Int. J. Coal Geol. 211, 103204. https://doi.org/10.1016/j.coal.2019.05.011.

Wang, G., Han, D.Y., Jiang, C.H., et al., 2020. Seepage characteristics of fracture and dead-end pore structure in coal at micro- and meso-scales. Fuel 266, 117058. https://doi.org/10.1016/j.fuel.2020.117058.

Wang, D.K., Zeng, F.C., Wei, J.P., et al., 2021a. Quantitative analysis of fracture dynamic evolution in coal subjected to uniaxial and triaxial compression loads based on industrial CT and fractal theory. J. Petrol. Sci. Eng. 196, 108051. https://doi.org/10.1016/j.petrol.2020.108051.

Wang, Y.D., Shabaninejad, M., Armstrong, R.T., et al., 2021b. Deep neural networks for improving physical accuracy of 2D and 3D multi-mineral segmentation of rock micro-CT images. Appl. Soft Comput. 10, 107185. https://doi.org/10.1016/j.asoc.2021.107185.

Wei, G.M., Wen, H., Deng, J., et al., 2021. Liquid CO_2 injection to enhance coalbed methane recovery: an experiment and in-situ application test. Fuel 284, 119034. https://doi.org/10.1016/j.fuel.2020.119043.

Wu, H., Yao, Y.B., Zhou, Y.F., et al., 2019a. Analyses of representative elementary volume for coal using X-ray μ-CT and FIB-SEM and its application in permeability predication model. Fuel 254, 115563. https://doi.org/10.1016/j.fuel.2019.05.146.

Wu, H., Zhou, Y.F., Yao, Y.B., et al., 2019b. Imaged based fractal characterization of microfracture structure in coal. Fuel 239, 53–62. https://doi.org/10.1016/j.fuel.2018.10.117.

Wu, Z.Q., Zhang, J., Fan, Y.J., et al., 2021. Synergistic effects from co-pyrolysis of lignocellulosic biomass with low-rank coal: a perspective based on the interaction of organic components. Fuel 306, 121648. https://doi.org/10.1016/j.fuel.2021.121648.

Xie, J., Gao, M.Z., Liu, J.J., et al., 2020. Permeability-enhanced rate model for coal permeability evolution and its application under various triaxial stress conditions. Arabian J. Geosci. 13 (17), 865. https://doi.org/10.1007/s12517-020-05777-x.

Yang, R., Liu, S.L., Wang, H.T., et al., 2021. Influence of H_2O on adsorbed CH_4 on coal displaced by CO_2 injection: implication for CO_2 sequestration in coal seam with enhanced CH_4 recovery (CO_2-ECBM). Ind. Eng. Chem. Res. 60 (43), 15817–15833. https://doi.org/10.1021/acs.iecr.1c03099.

Zeng, Q.S., Wang, Z.M., Sui, T.Y., et al., 2021. Adsorption mechanisms of high-pressure methane and carbon dioxide on coals. Energy Fuel. 35 (16), 13011–13021. https://doi.org/10.1021/acs.energyfuels.1c01094.

Zhang, G.L., Ranjith, P.G., Perera, M.S.A., et al., 2018. Characterization of coal porosity and permeability evolution by demineralisation using image processing techniques: a micro-computed tomography study. J. Nat. Gas Sci. Eng. 56, 384–396. https://doi.org/10.1016/j.jngse.2018.06.020.

Zhang, L., Jing, W., Yang, Y., et al., 2019a. The investigation of permeability calculation using digital core simulation technology. Energies 12 (17), 3273. https://doi.org/10.3390/en12173273.

Zhang, L., Li, J.H., Xue, J.H., et al., 2021a. Experimental studies on the changing characteristics of the gas flow capacity on bituminous coal in CO_2-ECBM and N_2-ECBM. Fuel 291, 120115. https://doi.org/10.1016/j.fuel.2020.120115/.

Zhang, X.D., Zhang, S., Du, Z.Q., et al., 2021b. CO_2 and N_2 adsorption/desorption effects and thermodynamic characteristics in confined coal. J. Petrol. Sci. Eng. 207, 109166. https://doi.org/10.1016/j.petrol.2021.109166.

Zhang, S., Zhang, X.D., Li, G.Z., et al., 2019b. Distribution characteristics and geochemistry mechanisms of carbon isotope of coalbed methane in central-southern Qinshui basin, China. Fuel 244, 1–12. https://doi.org/10.1016/j.fuel.2019.01.129.

Zheng, S.J., Yao, Y.B., Elsworth, D., et al., 2020. Dynamic fluid interactions during CO_2-ECBM and CO_2 sequestration in coal seams. Part 2: CO_2-H_2O wettability. Fuel 279, 118560. https://doi.org/10.1016/j.fuel.2020.118560.

Zhu, Q.Z., Wang, X.L., Zuo, Y.Q., et al., 2020. Numerical simulation of matrix swelling and its effects on fracture structure and permeability for a high-rank coal based on X-ray micro-CT image processing techniques. Energy Fuel. 34 (9), 10801–10809. https://doi.org/10.1021/acs.energyfuels.0c01903.